Biophysical Journal
Article

Molecular insights into the elevator-type mechanism of the cyanobacterial bicarbonate transporter BicA

Matthew C. Chan,[1] Yazeed Alfawaz,[1] Arnav Paul,[2] and Diwakar Shukla[1,2,3,4,5,*]
[1]Department of Chemical and Biomolecular Engineering, University of Illinois Urbana-Champaign, Urbana, Illinois; [2]Department of Chemistry, University of Illinois Urbana-Champaign, Urbana, Illinois; [3]Center for Biophysics and Quantitative Biology, University of Illinois Urbana-Champaign, Urbana, Illinois; [4]Department of Plant Biology, University of Illinois Urbana-Champaign, Urbana, Illinois; and [5]Department of Bioengineering, University of Illinois Urbana-Champaign, Urbana, Illinois

ABSTRACT Cyanobacteria are responsible for up to 80% of aquatic carbon dioxide fixation and have evolved a specialized carbon concentrating mechanism to increase photosynthetic yield. As such, cyanobacteria are attractive targets for synthetic biology and engineering approaches to address the demands of global energy security, food production, and climate change for an increasing world's population. The bicarbonate transporter BicA is a sodium-dependent, low-affinity, high-flux bicarbonate symporter expressed in the plasma membrane of cyanobacteria. Despite extensive biochemical characterization of BicA, including the resolution of the BicA crystal structure, the dynamic understanding of the bicarbonate transport mechanism remains elusive. To this end, we have collected over 1 ms of all-atom molecular dynamics simulation data of the BicA dimer to elucidate the structural rearrangements involved in the substrate transport process. We further characterized the energetics of the transition of BicA protomers and investigated potential mutations that are shown to decrease the free energy barrier of conformational transitions. In all, our study illuminates a detailed mechanistic understanding of the conformational dynamics of bicarbonate transporters and provides atomistic insights to engineering these transporters for enhanced photosynthetic production.

SIGNIFICANCE Cyanobacteria possess a unique CO_2-capturing mechanism that efficiently concentrates inorganic carbon into the cell to enable photorespiration. A component of this effective CO_2-capturing mechanism is the use of high-affinity, low-flux bicarbonate transporters expressed in the cyanobacteria plasma membrane. In this study, we performed large-scale molecular dynamics simulations of the cyanobacteria bicarbonate transporter BicA and provide a fully atomistic view of the structural rearrangements associated with bicarbonate transport. Our results present a mechanistic basis of how the activity of bicarbonate transporters may be enhanced and illuminate new solutions to address the increasing concerns of food security and climate change of a dynamic global population.

INTRODUCTION

Marine cyanobacteria, also known as green-blue algae, are estimated to contribute at least 30–80% of the Earth's total primary production (1,2). In aqueous solutions, carbon dioxide (CO_2) readily interconverts between carbonic acid (H_2CO_3) and bicarbonate ions (HCO_3^-). Unlike CO_2, HCO_3^- cannot freely diffuse through the plasma membrane and thus requires specialized integral membrane transporters to accumulate inorganic carbon for photosynthesis and carbohydrate production. Three bicarbonate transporters have been identified to be ubiquitously expressed in the cyanobacteria plasma membrane: BicA, a sodium-dependent, high-flux, low-affinity bicarbonate symporter; SbtA, a sodium-dependent, high-affinity symporter, and BCT1, a four-subunit bicarbonate transporter belonging to the ATP-binding cassette family (3,4) (Fig. 1 *A*). To date, the solved structure of BicA (5) (Fig. 1 *B*) and most recently of SbtA (6) have illuminated the molecular architecture of the overall topology and substrate binding site among these critical transporters.

In C3 crops, which include rice, barley, and wheat, carbon fixation via RuBisCo (ribulose-1,5-bisphosphate carboxylase/oxygenase) is notoriously known to be inefficient (7). As such, a possible approach to increases crop yield is to incorporate the efficient CO_2-capturing mechanisms utilized by cyanobacteria (8) into crops. Inorganic carbon transporters are one of two components that make up an effective

---

Submitted July 15, 2022, and accepted for publication December 10, 2024.

*Correspondence: diwakar@illinois.edu

Editor: Alan Grossfield.

https://doi.org/10.1016/j.bpj.2024.12.013

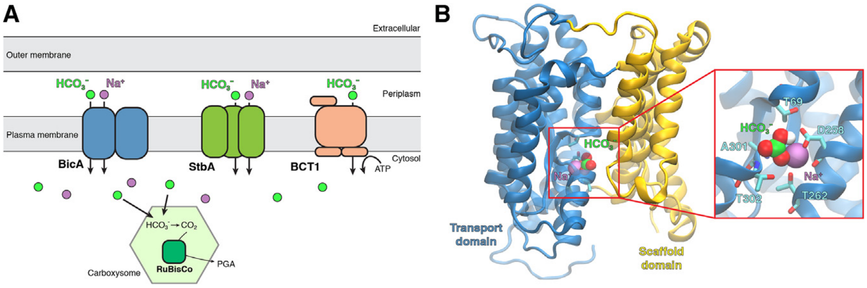

FIGURE 1 Cyanobacteria bicarbonate uptake transporters. (*A*) Schematic of select bicarbonate transporters expressed in the cyanobacteria plasma membrane. Transporters are depicted as follows: BicA, a sodium-dependent dimer (*blue*); StbA, a sodium-dependent trimer (*green*); BCT1, a four-subunit ATP-binding cassette transporter. Bicarbonate anions that are transported into the cytosol are then concentrated in the carboxysome, converted to carbon dioxide via carbonic anhydrase, and finally undergo photorespiration to form phosphoglyceric acid (PGA) via RuBisCo. (*B*) MD equilibrated structure of the BicA based on the crystal structure PDB: 6KI1. The cytoplasmic STAS domain is not shown for clarity. The transport domain and scaffold domain are colored blue and yellow, respectively. The bound substrates are represented as spheres. Residues that coordinate the binding of the substrates are shown as sticks.

CO_2-capturing mechanism, the other being the carboxysomes, which are specialized protein microcompartments that house RuBisCo and carbonic anhydrase to concentrate CO_2 for efficient carbon fixation (9). Kinetic modeling has proposed that introducing cyanobacteria bicarbonate transporters to the chloroplast of C3 crops may enhance photosynthetic yield by ~10%, while adding the carboxysome system may further increase yield as much as ~60% (10). Incorporating either bicarbonate transporters and the carboxysome involved the synthetic addition of foreign genes to the chloroplast of plastid genome. However, whereas bicarbonate transporters are simply encoded as single genes, the in vivo assembly of the carboxysome requires multiple proteins and presents inherent difficulties to simultaneously introduce all the required genes. As such, bicarbonate transporters are attractive candidates for engineering terrestrial crops to enhance inorganic carbon accumulation (11,12). In addition, increased carbon availability promotes cyanobacteria growth, which may be used for the production of biofuels and other bioproducts (13).

The cyanobacteria bicarbonate transporter BicA is a member of the solute carrier 26 (SLC26/SulP) family of anion transporters. Members of this family contain an N-terminal transmembrane (TM) domain comprised of 14 helices arranged in a 7 + 7 inverted repeat topology and a cytoplasmic C-terminal domain known as the sulfate transporter and anti-sigma factor antagonist, or STAS, domain (5). Despite low sequence conservation, transporters in the SLC4 and SLC23 families share the similar 7 + 7 TM architecture, but most notably lack the STAS domain (14). Furthermore, SLC26 transporters have been shown to adopt a unique dimer interface that involves TM helices 13 and 14, whereas TM helix 6 forms the dimer interface for SLC4 transporters, and TM helices 5 and 12 for SLC23 (15–17). Biophysical, structural, and computational studies (18–20) have illuminated the SLC26 family and similar related families to adopt a canonical alternating-access model in which the transporter undergoes a series of structural rearrangements to enable access of an orthosteric substrate binding site from either the extracellular or intracellular side (21–23). More specifically, the mode of transport of SLC26 transporters has been proposed to be an elevator-like mechanism (18,24,25), in which helices 1–4 and 8–11 form a mobile transport domain that translates across the membrane, thereby transporting substrates in and out of the cell (Fig. 1 *B*). TM helices 5–7 and 12–14 form the scaffold domain that remains rigid and is primarily involved in oligomeric assembly. Analogous SLC26 transporters in humans are involved in the exchange of anions throughout the body and mutations in these transporters are associated with various disorders such as cystic fibrosis, chloride diarrhea, and chondrodysplasia (26).

It is estimated that by 2050, the global food production must be doubled to sustain a growing population (27). To address the concern of global food security and sustainable energy, understanding the molecular mechanism of bicarbonate transport in cyanobacteria may serve as the basis for enhancing the efficiency of crop yield and biofuel production. While the resolved structure of BicA provides invaluable structural information, the conformational dynamics and energetics involved in the substrate translocation process may not be elucidated from a single structure and therefore remain elusive. With the recent surge in the computational efficiency of graphical processing units and numerical algorithms, molecular dynamics (MD) simulations combined with Markov state modeling (MSM) present a robust approach to characterize complex protein dynamics at atomistic resolution (28,29). Recent efforts in MSM have characterized the conformational heterogeneity of proteins of key interest to the plant biology community including phytohormone receptors (30–32), and circadian clock photoreceptors (33–35). Several membrane transporters have also been investigated using these methodologies including sugar transporters (SWEETs and SemiSWEETs) (36–38), bacterial nitrate transporters (39), human neurotransmitter (29,40), and peptide transporters (41). However, these transporters follow either the rocker-switch or rocking bundle mechanisms of alternate-access to facilitate the substrate transport (22,42). Members of the SLC26 anion carrier family have been observed to follow the elevator-type mechanism (16,43–45). We hypothesize that BicA has a similar mechanism as these transporters and follows the elevator-type

TABLE 1 Composition for pure cyanobacteria plasma membrane simulations

Lipid	Saturation (sn1/sn2)	Number of lipids per leaflet	Percentage (%)
MGDG	18:3γ/16:0	76	58
DGDG	18:3γ/16:0	21	16
SQDG	18:2/16:0	21	16
PG	18:2/16:0	6	5
PG	18:3α/16:0	6	5

mechanism (46–51), where the transport domain undergoes a translation relative to the scaffold domain to achieve alternate-access required for substrate transport (5).

In this study, we employed long-timescale all-atom MD simulations to provide a fully atomistic and dynamic perspective into the elevator-type bicarbonate transport mechanism of BicA. We further analyzed the simulation dataset using MSM (29) to quantify the thermodynamics of the elevator-type mechanism and its associated structural rearrangements. Finally, we investigated the effects of BicA mutations on the transporter structure and dynamics and present a mechanistic basis for mutations that may be introduced to BicA to enhance bicarbonate transport activity. Overall, our computational study provides an atomistic level perspective into the molecular mechanisms of BicA bicarbonate transport that may be used for further engineering of cyanobacteria and plants.

MATERIALS AND METHODS

MD simulations of pure cyanobacteria plasma membrane

To characterize the structural dynamics of BicA, we first sought to model a physiological membrane environment. Based on previous experimental characterization of cyanobacteria membranes, we constructed a symmetric lipid membrane containing the monogalactosyl diacylglycerol (MGDG), digalactosyl diacylglycerol (DGDG), sulfoquinovosyl diacylglycerol (SQDG), and phosphatidylglycerol (PG). The total number of each lipid species and lipid tail saturation are detailed in Table 1. A total of 130 lipid molecules per leaflet were assembled using PACKMOL (52). Water molecules and sodium ions to neutralize the system were further added. In all, the final MD membrane system contained 152 MGDG molecules, 42 DGDG molecules, 42 SQDG molecules, 24 PG molecules, 152 sodium ions, and 19,998 water molecules, totaling 140,834 atoms in a rectilinear box of 140 × 101 × 105 Å^3. A total of three membrane systems, randomizing the initial lipid placement, were constructed.

The MD systems were parameterized using the CHARMM36m force field (53). The parameters for the saturated lipids tails (18:3γ/16:0, 18:2/16:0, 18:3α/16:0), which are not originally parameterized in CHARMM36, were derived analogous from parameters of related lipid molecules in the CHARMM36 molecule set. The *psf* topology and coordinating file were created using the VMD psfgen plugin (54) and converted to AMBER *prmtop* topology and *rst7* coordinate files using the *chamber* module of the ParmEd package (55).

Simulations were performed on the AMBER18 package using the *pmemd* GPU accelerated module (56). The MD system was first minimized in 7000 steps using the steepest descent method followed by 93,000 steps using the conjugate gradient method. Before production simulations, the system was heated to 300 K in 100 K increments for 1 ns each while restraining the lipid headgroup atoms with a force constant of 1 kcal/mol-Å^2. Production simulations were performed in an NPT ensemble using Langevin dynamics with a damping coefficient of 1 ps^{-1} at 300 K, 1 bar, and positional restraints removed. A Monte Carlo barostat with an update interval of 100 steps was used to maintain pressure (57). A 12 Å distance cutoff was applied to calculate nonbonded interactions. Long-range electrostatic interactions were treated with the particle mesh Ewald method (58). Hydrogen bonds were constrained using the SHAKE algorithm (59). An integration timestep of 2 fs was used for membrane simulations. Each MD replicate was simulated for 250 ns with a trajectory frame saving rate of 100 ps.

We noted that a previous computational study identified errors in using a similar parameter combination of the Monte Carlo barostat and 12 Å hard cutoff (60). We have compared the dynamics of our lipid membrane with a 12 Å cutoff/10 Å switch versus just a 12 Å cutoff/no switch function. In both simulated setups, the membrane approaches equilibrium after ~50 ns (Fig. S1). For the 12 Å cutoff, we calculated the average membrane thickness to be 37.2 ± 0.3 Å and area-per-lipid (APL) of 58.8 ± 0.5 Å^2 (average ± standard deviation, over last 50 ns). In comparison, the 12 Å cutoff/10 Å switch resulted in an average membrane thickness of 36.5 ± 0.3 Å an APL of 61.4 ± 0.5 Å^2. Overall, we find that systems remain stable throughout the simulations, with small differences in the APL and membrane thickness between the two simulation parameters.

Modeling of the full-length BicA dimer system

The three-dimensional coordinates of the resolved BicA crystal structure (PDB: 6KI1, 6KI2) (5) were used as the starting structure for simulations. First, TM helix 14 was modeled based on the SLC26Dg structure (PDB: 5DA0) To model the full-length BicA dimer, two TM domains were aligned to the SLC26a9 murine transporter (16), in which TM helices 13 and 14 formed the dimeric interface (17). The STAS domain was placed under the TM domain and residues that linked the two domains were modeled with MODELLER (61). We found the resulting full-length BicA dimer to modestly fit in the cryo-EM map (5), which may be attributed to its low resolution or reconstruction in detergent. The modeled dimer, containing residues 2–547, was embedded in the cyanobacteria plasma membrane and solvated with TIP3P water molecules. Ten bicarbonate anions were randomly placed in the solvent and sodium ions were added to neutralize the system. Protonation states were assigned based on pKa calculations from PROPKA3.4 (62) and a system pH of 8 (5). Histidine residues were modeled as HSD. The final BicA dimer system consisted of 2 BicA protomers, 152 MGDG molecules, 42 DGDG molecules, 42 SQDG molecules, 24 PG molecules, 10 bicarbonate anions, 80 sodium ions, and 30,200 water molecules, totaling 141,886 atoms in a rectilinear box of 140.0 × 101.0 × 126.0 Å^3.

The alternative structure prediction of the BicA dimer was generated using AlphaFold v2.2.0 in tandem with the multimer mode (63,64). The AlphaFold prediction was performed using the following parameters: –max_template_date=2022-05-01; model_preset=multimer, –norun_relax, –db_preset=reduced_dbs. The output structure from AlphaFold was not used for simulations in this study.

MD simulations of the full-length BicA dimer

The BicA dimer system was parameterized using the CHARMM36m force field and conducted on the AMBER18 package (53,56). Before production simulation, the system was minimized for 5000 steps using the steepest descent method, followed by 45,000 steps using the conjugate gradient method. The BicA dimer was then subjected to 10 preproduction simulations with varying atoms restrained, totaling 150 ns. A detailed list of temperatures, restrained atoms, and simulation length for each preproduction step is presented in Table S1.

Production simulations were performed under the same conditions and parameters as the previous described pure membrane system, with the exception of the use of a 4 fs integration timestep and hydrogen mass repartition (65). To determine the stability of the full-length BicA dimer, a total of 7 simulations were initiated from the last preproduction step and simulated for 700 ns. The resulting trajectories from these simulations yielded BicA remaining in the inward-facing (IF) state. As such, to explore the conformational space of BicA, we adaptively sampled the conformational landscape based on the distances of the substrate to the binding sites and the displacement of the transport domain (29). The adaptive sampling scheme involves iteratively performing many independent simulations in parallel, followed by clustering the simulation data based on a geometric metric (66–68). Several different types of adaptive sampling approaches have been proposed in the literature (68–74). Here, we used least count-based sampling, where the subsequent round of adaptive sampling simulations is seeded from the least-populated clusters to maximize the probability of observing new conformations. It is one of the optimal sampling policies for efficient exploration of the conformational free energy landscapes (74,75). However, after 14 rounds of adaptive sampling, we did not observe either BicA protomer to transition from the IF state (Fig. S2). As such, we seeded subsequent rounds from a targeted MD trajectory, which simulated the transition from IF to outward-facing (OF) state (Fig. S6). The targeted MD simulation was performed using NAMD2.14 (76) using a 200 kcal/mol-Å^2 force constant and an OF/OF BicA homology model based on the NBCe1 cryo-EM structure (PDB: 6CAA) (77) as the target structure. A total of 29 adaptive rounds, in which individual trajectories were 60 ns long, were conducted and totaled 1.003 ms of aggregate simulation data (Table S2). Production simulations were performed on the Blue Waters supercomputer on Tesla K20 GPUs.

Trajectory analysis

Trajectories were processed with in-house scripts utilizing the CPPTRAJ, pytraj (78), and MDTraj (79) packages. Simulation trajectories were visualized using Visual Molecular Dynamics (VMD) 1.9.3 (54). Residue contact probabilities were calculated using the GetContacts (https://getcontacts.github.io/) Python package. Cross correlation analysis of BicA was performed using the Bio3D R package (80).

MSM

All 1.003 ms of aggregate simulation data from adaptive sampling simulations were used to construct a reversible MSM using the pyEMMA Python package (81). The simulation data were featurized based on the distances of residue pairs that were identified to uniquely form in the IF and OF states and determined using a residue-residue contact score (82). In all, 192 distances were identified between the two BicA protomers (Table S5). In addition, the z-components of Asp258 and the transported bicarbonate anion were included as features for the MSM, totaling 196 Cartesian features. The number of time-independent components and number of clusters were optimized using a grid search to maximize the VAMP1 score (Fig. S3 *A*). The best-scoring model was achieved with 10 time-independent components and 400 clusters. A lagtime of 10 ns was determined based on convergence of the implied timescales (Fig. S3 *B*). The standard error of the free energy landscape was calculated using the bootstrap method by randomly selecting 80% of the trajectories for 500 independent samples (Fig. S4). The reversibility of the MSM was assessed by comparing $\pi_i P_{ij} = \pi_j P_{ji}$ and the differences between $\pi_i P_{ij}$ and $\pi_j P_{ji}$ were within 10^{-15} (Fig. S5).

Umbrella sampling simulations

To investigate the energetics of conformational transitions of BicA mutants, we employed umbrella sampling simulations. The displacement between the z-component of the transport domain center of mass and the z-component of the scaffold domain center of mass was used as the reaction coordinate to describe the conformational transitions from IF to OF. Based on the conformational free energy landscape, one protomer of BicA is predicted to undergo transitions at once and, as such, we employed the umbrella sampling protocol on only BicA monomer A. Structures were drawn from the conformational landscape. A total of 26 windows from z-coordinates −8.0 to +4.5, in 0.5 Å intervals, were used to seed umbrella sampling simulations. Each window was simulated for 16 ns. Umbrella sampling simulations were performed using NAMD2.14 (76) using a 2 fs integration timestep, 12 Å cutoff, with a 10 Å switching distance, and a harmonic force constant of 15 kcal/mol-Å^2. Simulation frames were saved every 10 ps. Potentials of mean force (PMFs) were calculated using the multistate Bennett acceptance ratio as implemented by the pyMBAR python package (83). Secondary structure, computed by DSSP, remained intact throughout all umbrella windows (Fig. S7). Convergence and overlap matrices of umbrella sampling simulations are shown in (Figs. S8–S13).

Generation of multiple sequence alignments

Multiple sequence alignments were generated using the ConSurf web server (84). The sequences of BicA, UraA (PDB: 5XLS)(18), and NCBe1 (PBD: 6CAA) (77) were used as input to represent SLC26, SLC23, and SLC4 families. A 95% maximal identity between sequences and a 35% minimal identity between homologs was used to create the alignment. Three hundred represented sequences were sampled from the list of accepted homologs. Sequence logo figures were generated using the WebLogo server (85).

RESULTS AND DISCUSSION

Structural characterization of a full-length BicA dimer in a cyanobacteria plasma membrane

We sought to simulate a full-length model of BicA in a lipid membrane that best resembles the physiological plasma membrane of cyanobacteria. In addition to portraying a realistic molecular environment, the increased membrane complexity may also affect thermodynamics barriers across the conformational landscape (38). To this end, we constructed a lipid membrane based on previously characterized compositions determined for cyanobacteria (Fig. 2 *A*) (86,87). Notably, the cyanobacteria plasma membrane comprises mainly glycolipids. The constructed membrane consisted of the four unique and most abundant identified lipids: MGDG, DGDG, SQDG, and PG. The saturation of fatty acid tails was also modeled in accordance to Murata et al. (86). Further details of the composition of the simulated membrane are listed in Table 1.

To assess the dynamics of the cyanobacterial plasma membrane, all-atom MD simulations were performed using the AMBER18 engine (88) employing CHARMM36 force fields (89). Three independent replicates with unique initial lipid placement were constructed and simulated for 250 ns each. The simulated membrane readily approaches equilibrium after ~50 ns, with an average membrane thickness of 37.2 ± 0.3 Å and APL of 58.8 ± 0.5 Å^2 (average ± standard deviation, over last 50 ns) (Fig. 2, *B* and *C*). We find that the physical properties of our simulated membrane is in agreement with the compositionally similar

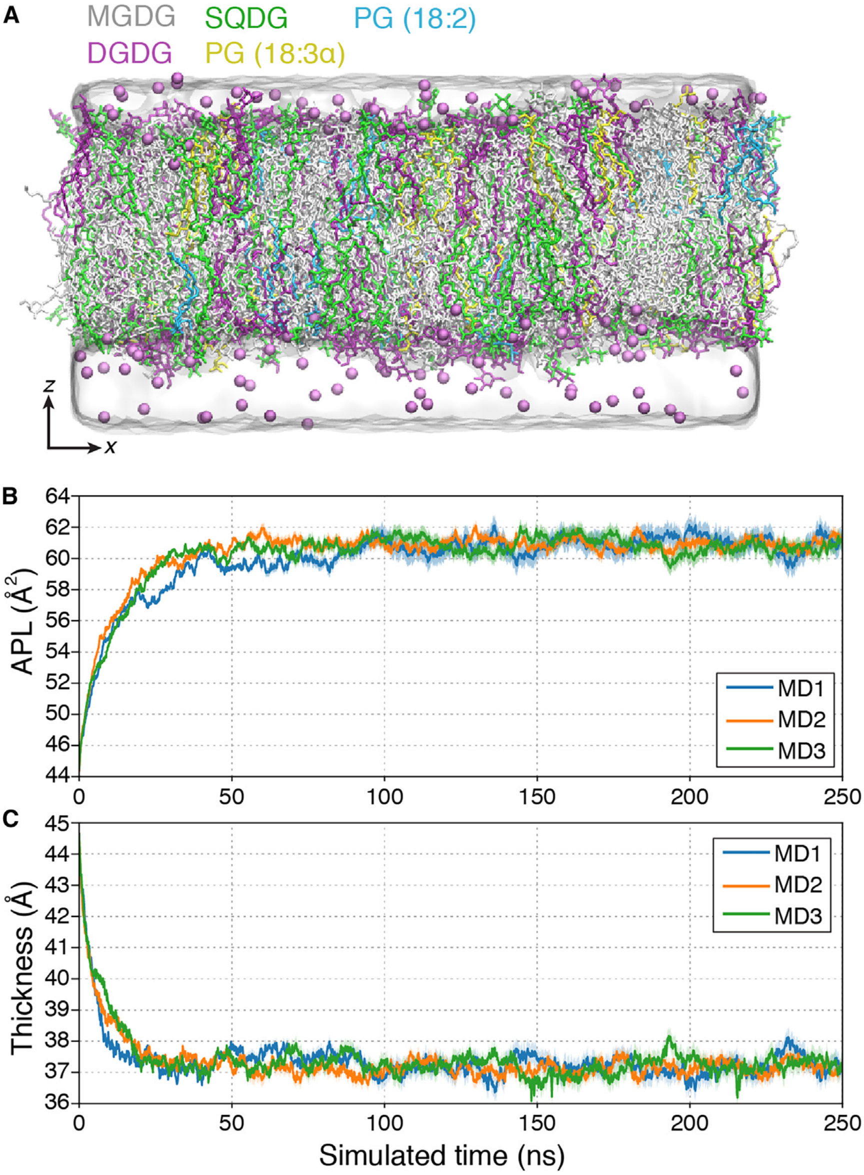

FIGURE 2 MD simulations of the cyanobacterial plasma membrane. (*A*) MD snapshot of the simulated cyanobacterial plasma membrane. Lipid molecules are shown as sticks and colored by individual lipid species. Sodium ions are represented as purple spheres. (*B* and *C*) Time-resolved measurements (*B*, area-per-lipid [APL] and *C*, membrane thickness) of the cyanobacterial lipid membrane. The three MD replicates are colored accordingly. Error bars represented accumulated standard deviation after the initial 50 ns.

cyanobacteria thylakoid membrane, previous characterized by simulation (90).

With the cyanobacteria plasma membrane established, we set to construct a full-length dimeric BicA system, using the resolved crystal structures of the TM domain (PDB: 6KI1) and the STAS domain (PDB: 6KI2) (5). Based on pulsed electron-electron double resonance spectroscopy (17) and the cryo-EM structure of the dimeric SLC26a9 murine transporter (16), the initial orientation of the two BicA protomers was placed where helices 13 and 14 formed the interface. We alternatively modeled a full-length BicA dimer structure using AlphaFold (63) and observed a similar orientation of the TM domains and its interface (Fig. S14). However, the structure predicted by AlphaFold did not model the STAS domain in accordance to the crystal structure or cryo-EM density (Fig. S14). As such, we proceeded with the BicA dimer structure based on the two available crystal structures and superposition of other SLC26 transporters. The full-length BicA dimer was embedded in the cyanobacteria plasma membrane and a total of seven MD replicates of 700 ns were performed (Fig. 3 *A*). During the preproduction stages of the simulations, we observed the one sodium ion to bind to one BicA monomer and remained bound throughout the 700 ns simulation across the seven replicates. The binding of a sodium ion to the remaining BicA monomer was observed within 200–500 ns of simulation (Fig. S15). In both cases, the sodium ion is coordinated by the side chains of Asp258, Thr262, and Thr302, consistent with the resolved crystal structure and previous mutagenesis characterization (5). The bicarbonate anion was not observed to bind in the substrate cavity within the equilibration timescales.

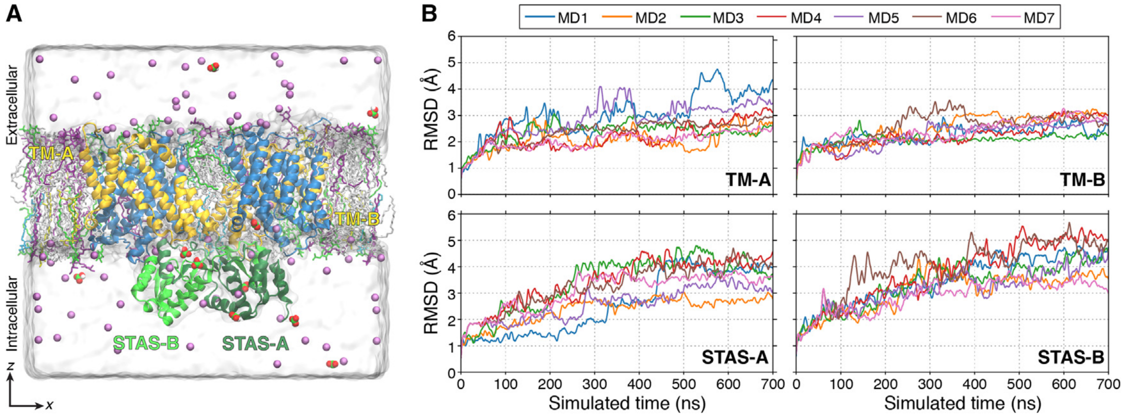

FIGURE 3 Stability of the full-length BicA dimer model. (*A*) MD snapshot of the full-length BicA dimer embedded in the cyanobacteria plasma membrane. Lipid molecules are shown as sticks and colored by lipid species as shown in Fig. 2 *A*. The BicA dimer is shown in cartoon representation and colored as follows: yellow, blue domain; blue, transport domain; green, STAS domain. Individual BicA protomers are labeled as A and B. Sodium ions are shown as purple spheres. Bicarbonate ions are shown as red and green spheres. (*B*) Time-resolved root mean-squared deviations (RMSD) of individual BicA transmembrane (TM) and STAS domains across the seven MD simulations. RMSD was calculated based on the starting structure of the 700 ns simulation. Individual MD replicates are colored accordingly.

The simulations reveal that the TM domains of BicA remain relatively stable (Cα RMSD < 3.5 Å), whereas the cytoplasmic STAS domain deviated from its initial structure (Cα RMSD > 3.5 Å) (Fig. 3 *B*). Moreover, upon equilibrating the full-length BicA system, we observed particularly the α2 helices to unwind and propagate the collapse of the domain. Indeed, the structural elements that form the STAS domain architecture are not maintained throughout the 700 ns long simulations (Fig. S16). The inherent differences between the simulated and experimentally determined structure may be attributed to artificial crystal contacts formed during crystallography or the lack of the TM domains being coexpressed to mediate the folding of the STAS domain. Functionally, the STAS domain of the sulfate transporter Sultr1;2 in *Arabidopsis thaliana* has been characterized to interact with cysteine synthase (O-acetylserine (thiol)lyase) to regulate the transporter function and mediate the cellular sulfur concentration (91). The association of the STAS domain with other regulatory proteins is further exhibited in the SLC26A3 transporter in humans with implications in cystic fibrosis (92). As such, it is likely that the STAS domain may adopt various conformations in solution and be stabilized upon association. We further simulated a BicA dimer with the STAS domains removed and did not observe difference in dimer stability of the TM domain (Fig. S17).

Structural requirements and energetics of BicA conformational transitions

As the timescales of large structural rearrangements and substrate transport may occur on the orders of microseconds or greater (93,94), observing these long timescale processes through conventional MD approaches may present inherent challenges in achieving adequate conformational sampling. As such, to simulate the bicarbonate transport process of BicA, we implemented a MSM-based adaptive sampling scheme to maximize the exploration of the conformational landscape (29). In brief, the adaptive sampling protocol is an iterative approach in which multiple simulations are conducted in parallel and then clustered using a K-means algorithm based on geometric criteria. To sample the BicA substrate translocation process, the distances between substrates and binding site and the *z*-component of the transport domain were chosen as the adaptive sampling metrics. To maximize the likelihood of exploring new conformations, structures from the least populated states are seeded for the subsequent round of simulation. Furthermore, to expedite the sampling, we seeded simulations from a targeted MD trajectory that captured the transition from IF to OF (Fig. S6). A total of 1.003 ms of aggregate simulation data was collected and used to construct an MSM (95). We note that the conformational sampling performed for this study simulates the export of bicarbonate to the extracellular side. Although BicA is responsible for concentrating inorganic carbon in the cell, the benefit of the MSM is representing the transport process as a reversible process and calculating the reversible transition probabilities between states, thereby capturing the bicarbonate import process.

By projecting the MSM-weighted simulation data on the reaction coordinates defined by the *z*-component of the Asp258 Cα atom (the residue that coordinates binding of the bicarbonate anion, Fig. 1 *B*), the conformational free energy landscape illustrates the cooperativity of the two BicA protomers (Fig. 4 *A*). IF conformations, in which the substrate binding site is accessible from the intracellular solvent (Fig. 4 *B*), are energetically stable with a relative free energy of 0–1 kcal/mol. Furthermore, the simulations reveal that the BicA protomer may independently undergo structural

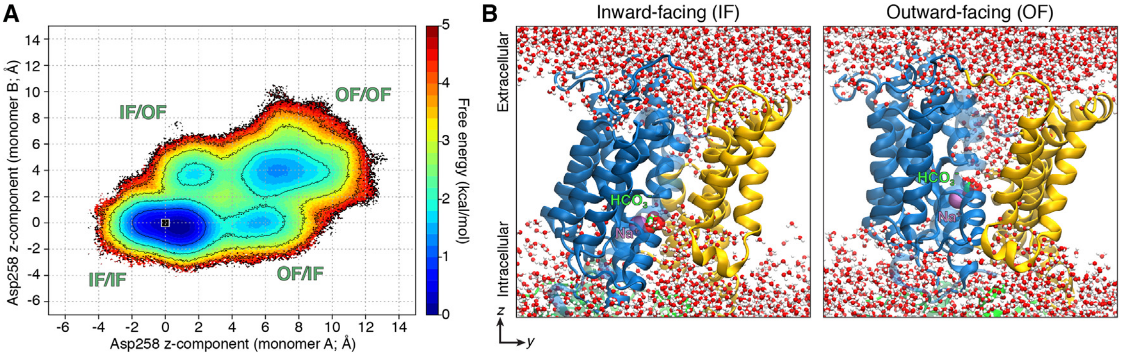

FIGURE 4 Energetics of BicA conformational transitions. (*A*) MSM-weighted conformational free energy landscape of BicA. The simulation data are projected on the axis defined by the *z*-component of the Cα atom of Asp258 for the respective BicA protomers. The displacement of Asp258 is measured with respect to the initial structure used for adaptive sampling simulations and indicated by the black square. Standard error measurement of the free energy landscape is presented in Fig. S4. (*B*) Representative MD snapshots of BicA showing the solvent accessibility of the substrate binding site in the inward-facing (IF) and outward-facing (OF) conformation. The transport domain is shown as blue cartoon, while the scaffold domain is colored in yellow. Water molecules are shown as red and white spheres. STAS domain not shown for clarity.

rearrangements to form OF states in which the transport domain has shifted ∼6 Å and the substrate binding site is now accessible to the extracellular space (Fig. 4 *B*). Similar to other transporters that adopt the elevator mechanism (96,97), the BicA transport domain simultaneously undergoes rotational and translational motion to fulfill alternate access (Fig. S21).

The free energy barrier associated with transitions from the IF to OF states for a single BicA protomer is estimated to be ∼2.5–3 kcal/mol (Figs. 4 *A* and S18). Based on the sampling seeded from the targeted MD trajectory, structures in which both BicA protomers form the OF conformation are stable with a relative free energy minima of ∼ 2 kcal/mol. However, the transition free energy barriers for the remaining BicA protomer to adopt the OF state, given that the other protomer is already OF, is ∼ 3–4 kcal/mol. Likewise, for both protomers to simultaneously transition to the OF state is estimated to be energetically less favored with free energy barriers of ∼4–5 kcal/mol (Fig. S18). We have seeded three simulations of BicA in the OF state and collected 700 ns of free dynamics in a similar manner as the IF simulations. Compared with the IF state simulations, we find similar RMSD deviations from the respective initial state and reveal that the OF conformation remains stable with an RMSD of 4 Å when compared with the initial OF state (Fig. S19). Our simulations were unable to capture strong coupling effects between the two BicA protomers during IF to OF transitions (Fig. S22 *A*). Estimation of the mean first passage time between conformational states identified the timescale for transition on the order of hundreds of microseconds (Table S3). The transition from IF/IF state to OF/OF state can happen via a simultaneous transition (670 μs) or a staggered pathway involving intermediate states. The timescale for a staggered transition is slightly faster that direct transition for the IF/IF to OF/IF to OF/OF pathway. Overall, the conformational free energy landscape suggests one protomer of BicA actively undergoes structural transitions in the dimeric state, consistent with previous studies of the SLC26Dg fumarate transporter (17,98).

We note the presence of two proline residues, Pro122 and Pro341, that flank the transport domain (Fig. 5 *A*). Sequence analysis reveals that, in 300 homologs, Pro341 is absolutely conserved, whereas Pro122 is substituted for Ser in a few homologs (Fig. 5 *B*). As the proline residue adopts a cyclic side chain that uniquely constrains the protein backbone, we hypothesized whether the steric effects provide the structural requirements for the conformational transitions of BicA. To investigate the effects of the proline residues on the transport dynamics, we implemented umbrella sampling simulations and calculated the PMF profiles of BicA to transition from IF to OF. The conformational free energy landscape suggest that BicA protomers can transition independently as well as simultaneously, with independent transitions being more favorable. As such, umbrella sampling simulations were initiated from MD snapshots of the BicA monomer A obtained from the adaptive sampling simulations. Umbrella sampling simulations were conducted with the NAMD2.14 package (76).

In the wild-type BicA system, the highest free energy barrier is associated with the transition to the OF state, with an estimated barrier of 3.75 ± 0.18 kcal/mol. When the Pro122 and Pro341 are mutated to glycine residues (Pro122Gly;Pro341Gly), we observed the stability of the OF state to be similar to that of the wild-type (wild-type: 3.40 ± 0.19 kcal/mol; Pro122Gly;Pro341Gly: 3.78 ± 0.18 kcal/mol), but the free energy barrier has now increased to 4.13 ± 0.14 kcal/mol (Fig. 5 *C*). Contrary to prolines, glycine residues provide innate flexibility of the peptide backbone given the lack of a heavy atom side chain. However, such flexibility did not provide necessary structural requirements to promote the formation of the OF state. We further simulated and calculated the PMF profile for the respective alanine mutant (Pro112Ala;Pro341Ala)

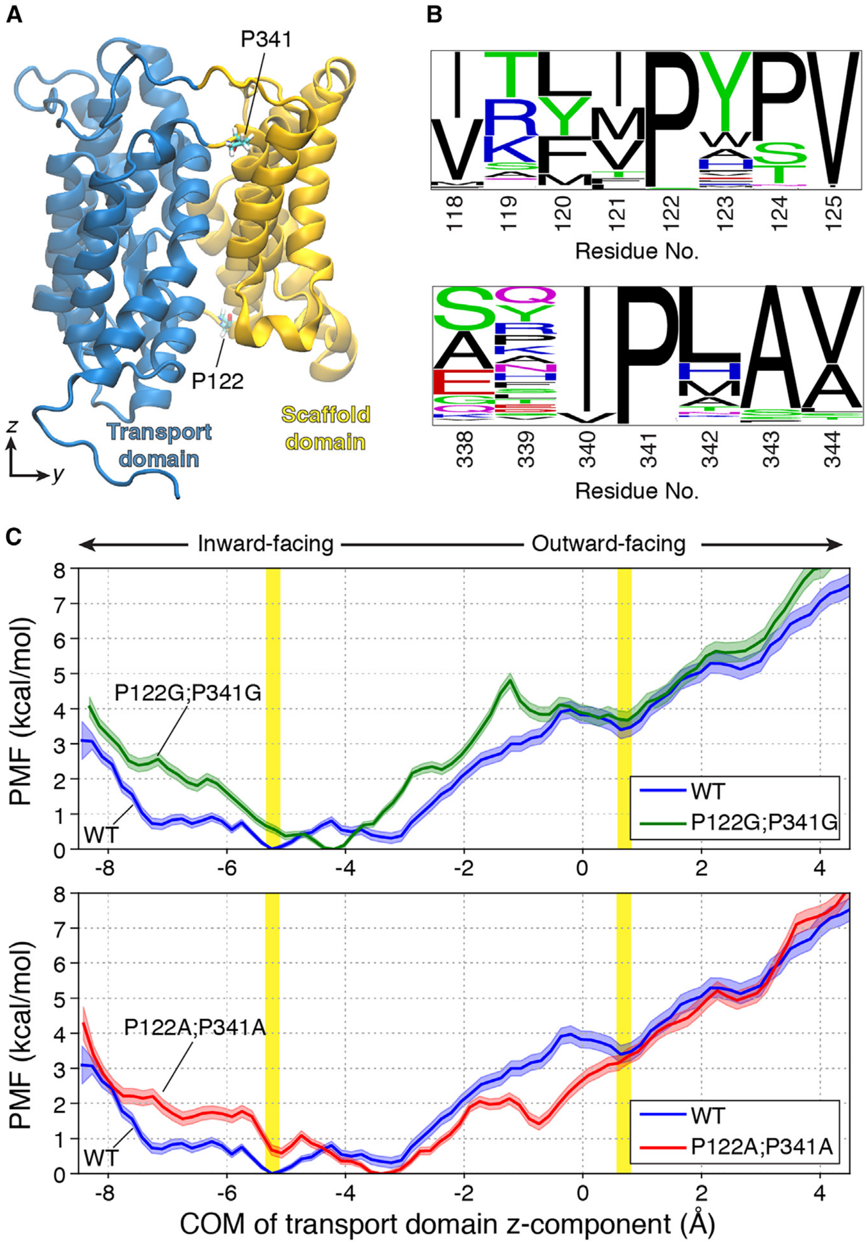

FIGURE 5 Conserved prolines residues flank the BicA transport domain. (*A*) Structure of the transmembrane domain of BicA, colored by transport and scaffold domain in blue and yellow respectively. Proline residues, P122 and P341, investigated are indicated and shown as sticks. (*B*) Sequence logo representation (85) of the proline and adjacent residues depicting the amino acid frequency of 300 homologs. Size of the amino acid font represents its respective frequency in the multiple sequence alignment. (*C*) Potentials of mean force (PMF) profiles for inward-facing to outward-facing transitions of wild-type (WT) and mutant BicA. BicA systems are colored as follows: blue, wild-type; green, P122G;P341G; red, P122A;P341A. *x* axis represents the *z*-coordinate displacement of the center of mass (COM) of the transport domain with respect to the center of mass of the scaffold domain. Inward- and outward-facing conformations are highlighted as vertical yellow bars. Error bars represents standard error.

and observed that the free energy barrier is reduced to 1.94 ± 0.10 kcal/mol (Fig. 5 *C*). Moreover, the Pro112Ala; Pro341Ala mutant stabilizes an intermediate OF state, but the complete OF state remains of similar stability (wild-type: 3.40 ± 0.19 kcal/mol; Pro122Ala;Pro341Ala: 3.33 ± 0.15 kcal/mol). As alanine residues enable more structural constraints on the backbone compared with the glycine residues, the PMF profiles suggest that unique dihedral constraints provided by proline residues facilitate the necessary structural rearrangements of the transport domain of BicA, although we cannot comment on how these mutants may affect transporter expression, biogenesis, folding, or stability. A recent study on the SLC23 transporter UraA mutated the equivalent proline residues and observed decrease transport function (99).

Hydrophobic interactions mediate closure of the transport domain

Membrane transporters adopt a canonical series of structural rearrangements that facilitate proper substrate transport across the membrane, otherwise known as the alternating access mechanism (100). As such, the substrate binding site is accessible to either the intracellular or extracellular space at a given time. Simulations of BicA reveal that the closure of the transporter from either side is facilitated by

A Inward-facing

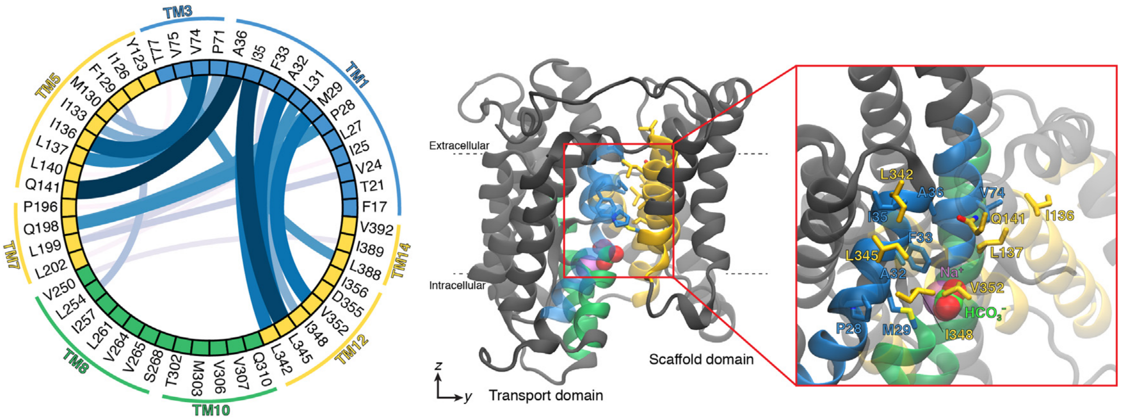

B Outward-facing

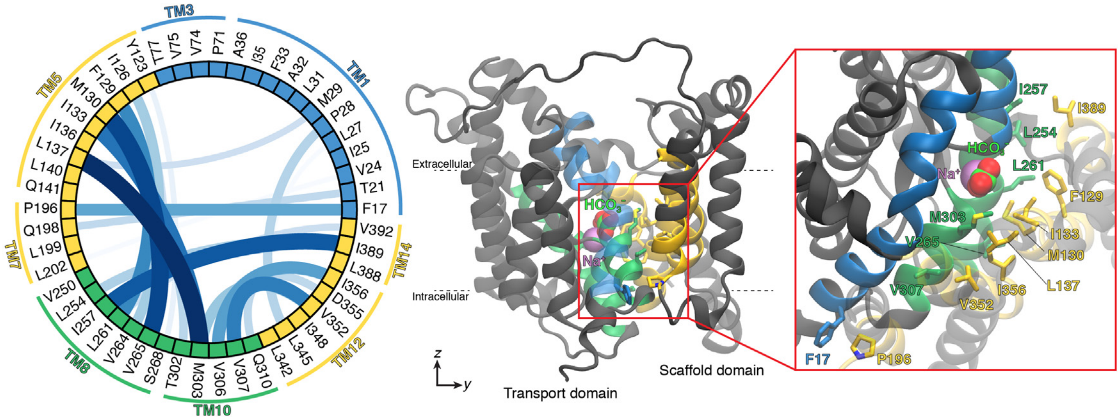

FIGURE 6 Hydrophobic gating residues of BicA. Chord diagram depicting the probability of interactions formed between gating residues in the (*A*) inward-facing conformation and (*B*) outward-facing conformation. Probability of interactions were calculated on 50,000 MD structures drawn from the respective free energy basin. Thickness and color intensity of connections between nodes represent the relative probability between two residues interacting. Accompanying MD snapshot showing selected residues mediating the closure of the transporter. STAS domain not shown for clarity. Transmembrane (TM) helices are colored as follows: blue, TM1, TM3; yellow, TM5, TM7, TM12, TM14; green, TM8, TM10.

hydrophobic residues that line the substrate translocation pathway (Fig. 6). Specifically, in the IF conformation, closure from the extracellular side is primarily mediated by TM helices 1 and 3 of the transport domain and helices 5, 7, 12, and 14 of the scaffold domain (Fig. 6 *A*). Upon substrate transport, as the transport domain shifts across the membrane, an intracellular gate is formed by residues on helices 8 and 10 with the scaffold domain (Fig. 6 *B*). As per the elevator-like mechanism, the scaffold domain serves as a shared gate between intracellular and extracellular residues. Furthermore, residues that comprise the hydrophobic gate are generally conserved among other transporters that adopt the 7 + 7 TM helix topology (Figs. S23 and S24). We expect that the hydrophobic residues in the respective positions of SLC4 and SLC23 transporters adopt a similar role in regulating the opening and closure of the transporter.

Given that the molecular gates of BicA are primarily facilitated by the hydrophobic interactions of aliphatic side chains, we sought to determine if mutations may be introduced to increase the substrate transport rate. Specifically, we hypothesized if substitutions to alanine residues may decrease the contacting surface area, while still retaining the nonpolar local environment to maintain proper transport function. To this end, we targeted residues with large aliphatic side chains (Met, Leu, Ile, etc.) located on various gating helices of BicA and residues of high contact probability based on the MD simulations. Three BicA triple mutants were simulated via the umbrella sampling protocol to delineate its effects on the energetics of the transporter conformational dynamics.

We first characterized mutations of residues on the hydrophobic gate that reside on the transport domain. The BicA triple mutant containing the substitutions Met29Ala;Phe33Ala;Ile35Ala are located on the extracellular half of TM helix 1 (Fig. 7, *top*). These residues were primarily found to interact with residues on TM12 to restrict access from the extracellular space and stabilize the IF conformation (Fig. 6 *A*). The PMF profile of the Met29Ala;Phe33Ala;Ile35Ala BicA mutant reveals the free energy barrier estimates to form the OF state has

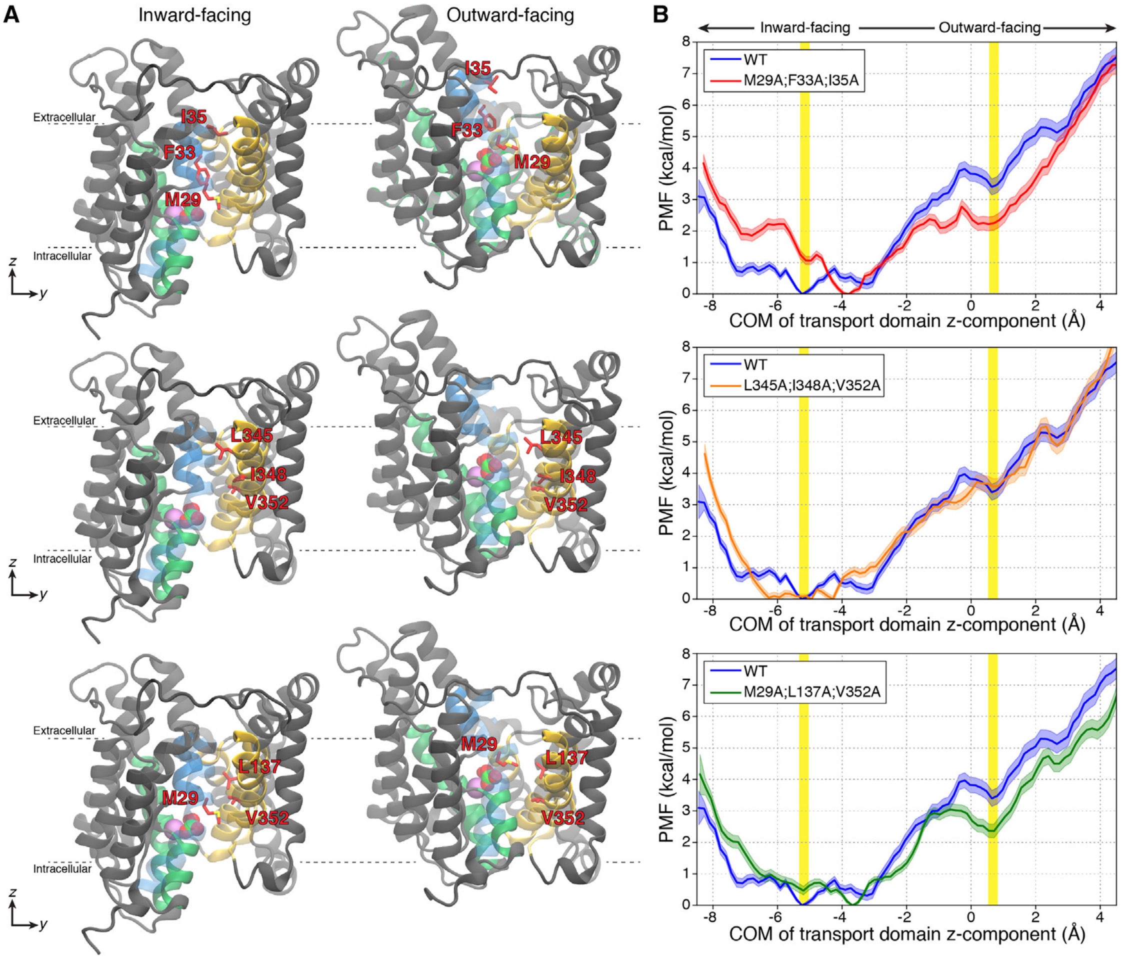

FIGURE 7 Simulated BicA triple mutants. (*A*) MD snapshots of the inward-facing and outward-facing conformations of BicA. Mutated residues are shown as sticks and colored red. The bicarbonate and sodium ion are shown as spheres and colored green and purple, respectively. Transmembrane (TM) helices are colored as follows: blue, TM1, TM3; yellow, TM5, TM7, TM12, TM14; green, TM8, TM10. STAS domain not shown for clarity. The mutants investigated in this study are Met29Ala;Phe33Ala;Ile35Ala (*top*), Leu345Ala;Ile348Ala;Val352Ala (*middle*), and Met29Ala;Leu137Ala,Val352Ala (*bottom*). (*B*) Potential of mean force (PMF) profiles of the three studied BicA triple mutants. The wild-type BicA is shown in blue and duplicated for comparison. BicA systems are colored as follows: blue, wild-type; red, Met29Ala;Phe33Ala;Ile35Ala; orange, Leu345Ala;Ile348Ala;Val352Ala; green, Met29Ala;Leu137Ala;Val352Ala. *x* axis represents the *z*-coordinate displacement of the center of mass (COM) of the transport domain with respect to the center of mass of the scaffold domain. Inward- and outward-facing conformations are highlighted as vertical yellow bars.

decreased to 2.50 ± 0.14 kcal/mol, as compared with the 3.75 ± 0.18 kcal/mol in wild-type BicA (Fig. 7, *top*). Furthermore, the relative free energy barrier estimate of OF to IF transitions remains similar to the wild-type (Met29Ala;Phe33Ala;Ile35Ala: 0.56 kcal/mol; wild-type: 0.58 kcal/mol) consistent that these residues are primarily responsible for extracellular closure and not predicted to directly affect the stability of the OF conformation.

The residues of the second BicA triple mutant, Leu345Ala;Ile348Ala;Val352Ala, are located on TM helix 12 of the scaffold domain (Fig. 7, *middle*). The PMF profiles for Leu345Ala;Ile348Ala;Val352Ala predict a modest decrease in the free energy barrier (Leu345Ala; Ile348Ala;Val352Ala: 3.37 ± 0.17 kcal/mol; wild-type: 3.75 ± 0.18 kcal/mol). We suspect that TM helix 12 serves as a shared gating helix that facilitate both IF and OF conformations and contributes to a slight favorable reduction in the free energy barrier. However, these mutations also compromise the destabilized interactions that close the intracellular pathway.

Lastly, the BicA mutant Met29Ala;Leu137Ala;Val352Ala targets residues on both the transport and scaffold domain (Fig. 7, *bottom*). This mutant was specifically simulated to remove the hydrophobic interactions involving Met29. In the IF state, Met29 interacts with Val352, whereas in the OF state Met29 switches its interaction partner to Leu137 (Fig. 6). Similar to the first described BicA triple mutant (Met29Ala;Phe33Ala;Ile35Ala), the PMF profile delineates a decrease in the free energy barrier (Met29Ala; Leu137AlaVal352Ala: 2.92 ± 0.13 kcal/mol; wild-type: 3.75 ± 0.18 kcal/mol) and similar stability of the OF state. In a multiple sequence alignment of 300 homologs generated by ConSurf, we find that the mutated residues are highly conserved in their physicochemical properties. The hydrophobic side chains of Met29, Ile35, and Ile348 are conserved, while Phe33 and Leu345 are entirely conserved. The MSA reveals that a population of BicA homologs have Thr in place of Val352 (Fig. S24). Overall, our simulations predict that alanine substitutions to residues on the TM domain, specifically TM helix 1, decrease the free energy barriers for structural rearrangements and are expected to increase bicarbonate uptake.

CONCLUSION

Bicarbonate transporters are key membrane transporters that regulate photosynthesis production. In this study, we utilized adaptive sampling and MSM to characterize the structural dynamics and thermodynamics of the BicA transport mechanism. Our simulations reveal that BicA protomers can undergo conformational transitions independently or simultaneously, consistent with previous cross-linking studies of the SLC26Dg transporter, where comparison of the transport activity of the active-active homodimer and the active-inactive heterodimer revealed that the active-active homodimer has slightly higher activity instead of double as expected (17). This suggests that, in the active-active homodimer, the protomer transitions are not always simultaneous and staggered transitions are slightly favored. In our simulations, we observed that the cytoplasmic STAS domain in the full-length BicA system remains folded and the complex formed between the STAS domains remains intact. However, the STAS domain complex undergoes large-scale rigid body motion in solution due to the presence of flexible linkers connecting it to the TM domains. We hypothesized that the stability of the STAS domain may be facilitated with other association proteins in vivo. Previous experimental characterization of the related *E. coli* YchM transporter has suggested the STAS domain to interact with a number of regulatory proteins with implications on transport activity (101). Further studies may focus on in vivo regulatory mechanisms of BicA.

We further investigated various BicA mutants that are predicted to affect the conformational energetics of the transport process. We predict that the unique steric constraints on the protein backbone provided by prolines residues located at junction of the scaffold and transport domain facilitate the proper conformational dynamics for transport. Furthermore, substitutions to bulky aliphatic residues that form the hydrophobic gate decrease the free energy barriers for IF to OF transitions. Specifically, alanine mutations located on TM helix 1 are predicted to enhance transport with minimal consequences on the stability of conformations. Such mutations to the hydrophobic gating residues introduced to the sodium/proton antiporter PaNhaP were also identified to increase transport activity (97). However, how these mutations may affect transporter expression, folding, trafficking, or biogenesis cannot be delineated from simulations. The elevator-type transitions of the dimeric BicA protomers is a slow and complicated dynamical process. The availability of only one resolved crystal structure in the IF state presents challenges in observing the full conformational cycle associated with the transport process. Modeling of complicated motions of elevator-type transporters often requires enhanced sampling methods such as targeted MD (tMD) to observe the transition pathway. Seeding of classical MD trajectories from the tMD trajectory may help sample all the relevant states involved during the transition; however, this method can bias the sampling toward one single transition pathway, which was discovered in the tMD run. To address this gap in knowledge, we preformed large-scale unbiased simulations (1 ms) using adaptive sampling to capture the full conformational landscape of the dimeric BicA. While we observed the slow transition timescales for BicA, our collected simulation dataset might not fully capture all possible conformations and transition pathways, especially those with higher free energy or separated by a large barrier from the initial pathway. In summary, using unbiased simulations, we were able to obtain relevant conformational states and observe transitions between these states and to estimate the thermodynamics and kinetics associated with bicarbonate transport. In all, the extensive simulations conducted in this study provide a comprehensive mechanistic view of BicA transport dynamics and elucidate potential engineered mutations to enhance cyanobacteria photosynthetic yield.

DATA AND CODE AVAILABILITY

Predicted OF state of BicA, lipid parameters, and structures extracted from the Markov state model are available on the Zenodo repository: https://doi.org/10.5281/zenodo.6647550. Molecular Dynamics trajectory files are available on box: https://uofi.box.com/s/tlejw02p66d50ybn4fndc5cq7dmc8dv6.

ACKNOWLEDGMENTS

This research was part of the Blue Waters sustained-petascale computing project, which was supported by the National Science Foundation (awards OCI-0725070 and ACI-1238993), the State of Illinois and, as of December, 2019, the National Geospatial-Intelligence Agency. Blue Waters was a joint effort of the University of Illinois Urbana-Champaign and its National Center for Supercomputing Applications. D.S. acknowledges funding from the NSF CAREER Award MCB-1845606 and funding from the National Institutes of General Medical Sciences Award R35GM142745.

AUTHOR CONTRIBUTIONS

D.S. acquired funding. D.S. supervised the study. M.C.C. and D.S. designed the study. M.C.C. and Y.A. performed simulations. M.C.C., Y.A., A.P., and D.S. analyzed the data. M.C.C. and A.P. wrote the manuscript with input from D.S. All authors reviewed the final manuscript.

DECLARATION OF INTERESTS

The authors declare no competing interests.

SUPPORTING MATERIAL

Supporting material can be found online at https://doi.org/10.1016/j.bpj.2024.12.013.

REFERENCES

1. Liu, H., H. A. Nolla, and L. Campbell. 1997. Prochlorococcus growth rate and contribution to primary production in the equatorial and subtropical North Pacific Ocean. *Aquat. Microb. Ecol.* 12:39–47.
2. Partensky, F., W. R. Hess, and D. Vaulot. 1999. Prochlorococcus, a marine photosynthetic prokaryote of global significance. *Microbiol. Mol. Biol. Rev.* 63:106–127.
3. Price, G. D., F. J. Woodger, …, L. Tucker. 2004. Identification of a SulP-type bicarbonate transporter in marine cyanobacteria. *Proc. Natl. Acad. Sci. USA.* 101:18228–18233.
4. Price, G. D. 2011. Inorganic carbon transporters of the cyanobacterial CO 2 concentrating mechanism. *Photosynth. Res.* 109:47–57.
5. Wang, C., B. Sun, …, P. Zhang. 2019. Structural mechanism of the active bicarbonate transporter from cyanobacteria. *Nat. Plants.* 5:1184–1193. https://doi.org/10.1038/s41477-019-0538-1.
6. Liu, X.-Y., W.-T. Hou, …, C.-Z. Zhou. 2021. Structures of cyanobacterial bicarbonate transporter SbtA and its complex with PII-like SbtB. *Cell Discov.* 7:63.
7. Bracher, A., S. M. Whitney, …, M. Hayer-Hartl. 2017. Biogenesis and metabolic maintenance of Rubisco. *Annu. Rev. Plant Biol.* 68:29–60.
8. Rae, B. D., B. M. Long, …, A. J. McCormick. 2017. Progress and challenges of engineering a biophysical CO2-concentrating mechanism into higher plants. *J. Exp. Bot.* 68:3717–3737.
9. Badger, M. R., and G. D. Price. 2003. CO2 concentrating mechanisms in cyanobacteria: molecular components, their diversity and evolution. *J. Exp. Bot.* 54:609–622.
10. McGrath, J. M., and S. P. Long. 2014. Can the cyanobacterial carbon-concentrating mechanism increase photosynthesis in crop species? A theoretical analysis. *Plant Physiol.* 164:2247–2261.
11. Du, J., B. Förster, …, G. D. Price. 2014. Characterisation of cyanobacterial bicarbonate transporters in E. coli shows that SbtA homologs are functional in this heterologous expression system. *PLoS One.* 9:e115905.
12. Rolland, V., M. R. Badger, and G. D. Price. 2016. Redirecting the cyanobacterial bicarbonate transporters BicA and SbtA to the chloroplast envelope: soluble and membrane cargos need different chloroplast targeting signals in plants. *Front. Plant Sci.* 7:185.
13. Gupta, J. K., P. Rai, …, S. Srivastava. 2020. Overexpression of bicarbonate transporters in the marine cyanobacterium Synechococcus sp. PCC 7002 increases growth rate and glycogen accumulation. *Biotechnol. Biofuels.* 13:1–12.
14. Chang, Y.-N., and E. R. Geertsma. 2017. The novel class of seven transmembrane segment inverted repeat carriers. *Biol. Chem.* 398:165–174.
15. Gorbunov, D., M. Sturlese, …, D. Oliver. 2014. Molecular architecture and the structural basis for anion interaction in prestin and SLC26 transporters. *Nat. Commun.* 5:3622.
16. Walter, J. D., M. Sawicka, and R. Dutzler. 2019. Cryo-EM structures and functional characterization of murine Slc26a9 reveal mechanism of uncoupled chloride transport. *Elife.* 8:e46986.
17. Chang, Y.-N., E. A. Jaumann, …, E. R. Geertsma. 2019. Structural basis for functional interactions in dimers of SLC26 transporters. *Nat. Commun.* 10:2032. https://doi.org/10.1038/s41467-019-10001-w.
18. Yu, X., G. Yang, …, N. Yan. 2017. Dimeric structure of the uracil:proton symporter UraA provides mechanistic insights into the SLC4/23/26 transporters. *Cell Res.* 27:1020–1033. https://doi.org/10.1038/cr.2017.83.
19. Wang, W., K. Tsirulnikov, …, I. Kurtz. 2021. Cryo-EM structure of the sodium-driven chloride/bicarbonate exchanger NDCBE. *Nat. Commun.* 12:5690. https://doi.org/10.1038/s41467-021-25998-2.
20. Coudray, N., S. L Seyler, …, D. L. Stokes. 2017. Structure of the SLC4 transporter Bor1p in an inward-facing conformation. *Protein Sci.* 26:130–145.
21. Jardetzky, O. 1966. Simple allosteric model for membrane pumps. *Nature.* 211:969–970.
22. Beckstein, O., and F. Naughton. 2022. General principles of secondary active transporter function. *Biophys. Rev.* 3:011307. https://doi.org/10.1063/5.0047967.
23. Drew, D., and O. Boudker. 2024. Ion and lipid orchestration of secondary active transport. *Nature.* 626:963–974.
24. Omori, S., Y. Hanazono, …, K. Kinoshita. 2024. The Role of the STAS domain in SLC26A9 for Chloride Ion Transporter Function. *Biophys. J.* 123:1751–1762.
25. Kuwabara, M. F., B. G. Haddad, …, D. Oliver. 2023. Elevator-like movements of prestin mediate outer hair cell electromotility. *Nat. Commun.* 14:7145.
26. Alper, S. L., and A. K. Sharma. 2013. The SLC26 gene family of anion transporters and channels. *Mol. Aspect. Med.* 34:494–515.
27. Long, S. P., A. Marshall-Colon, and X.-G. Zhu. 2015. Meeting the global food demand of the future by engineering crop photosynthesis and yield potential. *Cell.* 161:56–66.
28. Hollingsworth, S. A., and R. O. Dror. 2018. Molecular Dynamics Simulation for All. *Neuron.* 99:1129–1143. https://doi.org/10.1016/j.neuron.2018.08.011.
29. Chan, M. C., and D. Shukla. 2021. Markov state modeling of membrane transport proteins. *J. Struct. Biol.* 213:107800. https://doi.org/10.1016/j.jsb.2021.107800.
30. Chen, J., A. White, …, D. Shukla. 2021. Role of substrate recognition in modulating strigolactone receptor selectivity in witchweed. *J. Biol. Chem.* 297:101092. https://doi.org/10.1016/j.jbc.2021.101092.
31. Shukla, S., C. Zhao, and D. Shukla. 2019. Dewetting Controls Plant Hormone Perception and Initiation of Drought Resistance Signaling. *Structure.* 27:692–702.e3. https://doi.org/10.1016/j.str.2018.12.005.
32. Moffett, A. S., K. W. Bender, …, D. Shukla. 2017. Molecular dynamics simulations reveal the conformational dynamics of Arabidopsis thaliana BRI1 and BAK1 receptor-like kinases. *J. Biol. Chem.* 292:12643–12652. https://doi.org/10.1074/jbc.m117.792762.
33. Zhou, H., Z. Dong, …, P. Tao. 2019. Allosteric mechanism of the circadian protein Vivid resolved through Markov state model and machine learning analysis. *PLoS Comput. Biol.* 15:e1006801. https://doi.org/10.1371/journal.pcbi.1006801.
34. Zhao, Y., Y. Zhang, …, Q. Zheng. 2021. A theoretical study on the signal transduction process of bacterial photoreceptor PpSB1 based on the Markov state model. *Phys. Chem. Chem. Phys.* 23:2398–2405. https://doi.org/10.1039/d0cp05532h.
35. Trozzi, F., F. Wang, …, P. Tao. 2021. Dimeric allostery mechanism of the plant circadian clock photoreceptor ZEITLUPE. *PLoS Comput. Biol.* 17:e1009168. https://doi.org/10.1371/journal.pcbi.1009168.
36. Selvam, B., Y.-C. Yu, …, D. Shukla. 2019. Molecular Basis of the Glucose Transport Mechanism in Plants. *ACS Cent. Sci.* 5:1085–1096. https://doi.org/10.1021/acscentsci.9b00252.
37. Cheng, K. J., B. Selvam, …, D. Shukla. 2019. Distinct Substrate Transport Mechanism Identified in Homologous Sugar Transporters. *J. Phys. Chem. B.* 123:8411–8418. https://doi.org/10.1021/acs.jpcb.9b08257.
38. Weigle, A. T., M. Carr, and D. Shukla. 2021. Impact of Increased Membrane Realism on Conformational Sampling of Proteins. *J. Chem. Theor. Comput.* 17:5342–5357. https://doi.org/10.1021/acs.jctc.1c00276.
39. Feng, J., B. Selvam, and D. Shukla. 2021. How do antiporters exchange substrates across the cell membrane? An atomic-level description of the complete exchange cycle in NarK. *Structure.* 29:922–933.e3. https://doi.org/10.1016/j.str.2021.03.014.

40. Chan, M. C., E. Procko, and D. Shukla. 2022. Structural Rearrangement of the Serotonin Transporter Intracellular Gate Induced by Thr276 Phosphorylation. *ACS Chem. Neurosci.* 13:933–945. https://doi.org/10.1021/acschemneuro.1c00714.
41. Selvam, B., S. Mittal, and D. Shukla. 2018. Free Energy Landscape of the Complete Transport Cycle in a Key Bacterial Transporter. *ACS Cent. Sci.* 4:1146–1154. https://doi.org/10.1021/acscentsci.8b00330.
42. Drew, D., and O. Boudker. 2016. Shared Molecular Mechanisms of Membrane Transporters. *Annu. Rev. Biochem.* 85:543–572. https://doi.org/10.1146/annurev-biochem-060815-014520.
43. Tippett, D. N., C. Breen, …, R. Dutzler. 2023. Structural and functional properties of the transporter SLC26A6 reveal mechanism of coupled anion exchange. *Elife.* 12:RP87178.
44. Chang, Y.-N., E. A. Jaumann, …, E. R. Geertsma. 2019. Structural basis for functional interactions in dimers of SLC26 transporters. *Nat. Commun.* 10:2032.
45. Chi, X., X. Jin, …, X. Pan. 2020. Structural insights into the gating mechanism of human SLC26A9 mediated by its C-terminal sequence. *Cell Discov.* 6:55.
46. Matsuoka, R., R. Fudim, …, D. Drew. 2022. Structure, mechanism and lipid-mediated remodeling of the mammalian Na+/H+ exchanger NHA2. *Nat. Struct. Mol. Biol.* 29:108–120. https://doi.org/10.1038/s41594-022-00738-2.
47. Winkelmann, I., R. Matsuoka, …, D. Drew. 2020. Structure and elevator mechanism of the mammalian sodium/proton exchanger NHE9. *EMBO J.* 39:4541–4559. https://doi.org/10.15252/embj.2020105908.
48. Lee, C., H. J. Kang, …, D. Drew. 2013. A two-domain elevator mechanism for sodium/proton antiport. *Nature.* 501:573–577. https://doi.org/10.1038/nature12484.
49. Coincon, M., P. Uzdavinys, …, D. Drew. 2016. Crystal structures reveal the molecular basis of ion translocation in sodium/proton antiporters. *Nat. Struct. Mol. Biol.* 23:248–255. https://doi.org/10.1038/nsmb.3164.
50. Dong, Y., Y. Gao, …, Y. Zhao. 2021. Structure and mechanism of the human NHE1-CHP1 complex. *Nat. Commun.* 12:3474. https://doi.org/10.1038/s41467-021-23496-z.
51. Ruan, Y., A. Miyagi, …, S. Scheuring. 2017. Direct visualization of glutamate transporter elevator mechanism by high-speed AFM. *Proc. Natl. Acad. Sci. USA.* 114:1584–1588. https://doi.org/10.1073/pnas.1616413114.
52. Martínez, L., R. Andrade, …, J. M. Martínez. 2009. PACKMOL: A package for building initial configurations for molecular dynamics simulations. *J. Comput. Chem.* 30:2157–2164. https://doi.org/10.1002/jcc.21224.
53. Huang, J., S. Rauscher, …, A. D. MacKerell, Jr. 2017. CHARMM36m: an improved force field for folded and intrinsically disordered proteins. *Nat. Methods.* 14:71–73.
54. Humphrey, W., A. Dalke, and K. Schulten. 1996. VMD: visual molecular dynamics. *J. Mol. Graph.* 14:33–38.
55. Shirts, M. R., C. Klein, …, E. D. Zhong. 2017. Lessons learned from comparing molecular dynamics engines on the SAMPL5 dataset. *J. Comput. Aided Mol. Des.* 31:147–161.
56. Case, D., I. Ben-Shalom, P. Kollman…, 2018. Amber 2018. University of California.
57. Åqvist, J., P. Wennerström, …, B. O. Brandsdal. 2004. Molecular dynamics simulations of water and biomolecules with a Monte Carlo constant pressure algorithm. *Chem. Phys. Lett.* 384:288–294.
58. Essmann, U., L. Perera, …, L. G. Pedersen. 1995. A smooth particle mesh Ewald method. *J. Chem. Phys.* 103:8577–8593.
59. Kräutler, V., W. F. Van Gunsteren, and P. H. Hünenberger. 2001. A fast SHAKE algorithm to solve distance constraint equations for small molecules in molecular dynamics simulations. *J. Comput. Chem.* 22:501–508.
60. Gomez, Y. K., A. M. Natale, …, M. Grabe. 2022. Taking the Monte-Carlo gamble: How not to buckle under the pressure. *J. Comput. Chem.* 43:431–434. https://doi.org/10.1002/jcc.26798.
61. Webb, B., and A. Sali. 2016. Comparative Protein Structure Modeling Using MODELLER. *Curr. Protoc. Bioinformatics.* 54:5.6.1–5.6.37. https://doi.org/10.1002/cpbi.3.
62. Olsson, M. H. M., C. R. Søndergaard, …, J. H. Jensen. 2011. PROPKA3: consistent treatment of internal and surface residues in empirical p K a predictions. *J. Chem. Theor. Comput.* 7:525–537.
63. Jumper, J., R. Evans, …, D. Hassabis. 2021. Highly accurate protein structure prediction with AlphaFold. *Nature.* 596:583–589. https://doi.org/10.1038/s41586-021-03819-2.
64. Evans, R., M. O'Neill, …, D. Hassabis. 2021. Protein complex prediction with AlphaFold-Multimer. Preprint at bioRxiv. https://doi.org/10.1101/2021.10.04.463034.
65. Hopkins, C. W., S. Le Grand, …, A. E. Roitberg. 2015. Long-time-step molecular dynamics through hydrogen mass repartitioning. *J. Chem. Theor. Comput.* 11:1864–1874.
66. Hinrichs, N. S., and V. S. Pande. 2007. Calculation of the distribution of eigenvalues and eigenvectors in Markovian state models for molecular dynamics. *J. Chem. Phys.* 126:244101. https://doi.org/10.1063/1.2740261.
67. Bowman, G. R., D. L. Ensign, and V. S. Pande. 2010. Enhanced Modeling via Network Theory: Adaptive Sampling of Markov State Models. *J. Chem. Theor. Comput.* 6:787–794. https://doi.org/10.1021/ct900620b.
68. Kleiman, D. E., H. Nadeem, and D. Shukla. 2023. Adaptive Sampling Methods for Molecular Dynamics in the Era of Machine Learning. *J. Phys. Chem. B.* 127:10669–10681. https://doi.org/10.1021/acs.jpcb.3c04843.
69. Kleiman, D. E., and D. Shukla. 2023. Active Learning of the Conformational Ensemble of Proteins Using Maximum Entropy VAMPNets. *J. Chem. Theor. Comput.* 19:4377–4388. https://doi.org/10.1021/acs.jctc.3c00040.
70. Kleiman, D. E., and D. Shukla. 2022. Multiagent Reinforcement Learning-Based Adaptive Sampling for Conformational Dynamics of Proteins. *J. Chem. Theor. Comput.* 18:5422–5434. https://doi.org/10.1021/acs.jctc.2c00683.
71. Shamsi, Z., K. J. Cheng, and D. Shukla. 2018. Reinforcement Learning Based Adaptive Sampling: REAPing Rewards by Exploring Protein Conformational Landscapes. *J. Phys. Chem. B.* 122:8386–8395. https://doi.org/10.1021/acs.jpcb.8b06521.
72. Shamsi, Z., A. S. Moffett, and D. Shukla. 2017. Enhanced unbiased sampling of protein dynamics using evolutionary coupling information. *Sci. Rep.* 7:12700. https://doi.org/10.1038/s41598-017-12874-7.
73. Zimmerman, M. I., and G. R. Bowman. 2015. FAST Conformational Searches by Balancing Exploration/Exploitation Trade-Offs. *J. Chem. Theor. Comput.* 11:5747–5757. https://doi.org/10.1021/acs.jctc.5b00737.
74. Weber, J. K., and V. S. Pande. 2011. Characterization and Rapid Sampling of Protein Folding Markov State Model Topologies. *J. Chem. Theor. Comput.* 7:3405–3411. https://doi.org/10.1021/ct2004484.
75. Nadeem, H., and D. Shukla. 2024. Optimizing adaptive sampling via Policy Ranking. Preprint at arXiv. https://doi.org/10.48550/ARXIV.2410.15259.
76. Phillips, J. C., D. J. Hardy, …, E. Tajkhorshid. 2020. Scalable molecular dynamics on CPU and GPU architectures with NAMD. *J. Chem. Phys.* 153:044130. https://doi.org/10.1063/5.0014475.
77. Huynh, K. W., J. Jiang, …, I. Kurtz. 2018. CryoEM structure of the human SLC4A4 sodium-coupled acid-base transporter NBCe1. *Nat. Commun.* 9:900. https://doi.org/10.1038/s41467-018-03271-3.
78. Roe, D. R., and T. E. Cheatham. 2013. PTRAJ and CPPTRAJ: Software for Processing and Analysis of Molecular Dynamics Trajectory Data. *J. Chem. Theor. Comput.* 9:3084–3095. https://doi.org/10.1021/ct400341p.

79. McGibbon, R. T., K. A. Beauchamp, …, V. S. Pande. 2015. MDTraj: A Modern Open Library for the Analysis of Molecular Dynamics Trajectories. *Biophys. J.* 109:1528–1532. http://www.sciencedirect.com/science/article/pii/S0006349515008267.
80. Grant, B. J., A. P. C. Rodrigues, …, L. S. D. Caves. 2006. Bio3d: an R package for the comparative analysis of protein structures. *Bioinformatics.* 22:2695–2696.
81. Scherer, M. K., B. Trendelkamp-Schroer, …, F. Noé. 2015. PyEMMA 2: A Software Package for Estimation, Validation, and Analysis of Markov Models. *J. Chem. Theor. Comput.* 11:5525–5542. https://doi.org/10.1021/acs.jctc.5b00743.
82. Zhou, Q., D. Yang, …, S. Zhao. 2019. Common activation mechanism of class A GPCRs. *Elife.* 8:e50279. https://doi.org/10.7554/elife.50279.
83. Shirts, M. R., and J. D. Chodera. 2008. Statistically optimal analysis of samples from multiple equilibrium states. *J. Chem. Phys.* 129:124105.
84. Ashkenazy, H., S. Abadi, …, N. Ben-Tal. 2016. ConSurf 2016: an improved methodology to estimate and visualize evolutionary conservation in macromolecules. *Nucleic Acids Res.* 44:W344–W350.
85. Crooks, G. E., G. Hon, …, S. E. Brenner. 2004. WebLogo: a sequence logo generator. *Genome Res.* 14:1188–1190.
86. Murata, N., H. Wada, and Z. Gombos. 1992. Modes of Fatty-Acid Desaturation in Cyanobacteria. *Plant Cell Physiol.* 33:933–941. https://doi.org/10.1093/oxfordjournals.pcp.a078344.
87. Wada, H., and N. Murata. 1998. Membrane lipids in cyanobacteria. *In* Lipids in Photosynthesis: Structure, Function and Genetics Springer, pp. 65–81.
88. Case, D. A., I. Ben-Shalom, …, P. A. Kollman. 2018. AMBER 2018. University of California, San Francisco.
89. Klauda, J. B., R. M. Venable, …, R. W. Pastor. 2010. Update of the CHARMM All-Atom Additive Force Field for Lipids: Validation on Six Lipid Types. *J. Phys. Chem. B.* 114:7830–7843.
90. van Eerden, F. J., D. H. de Jong, …, S. J. Marrink. 2015. Characterization of thylakoid lipid membranes from cyanobacteria and higher plants by molecular dynamics simulations. *Biochim. Biophys. Acta.* 1848:1319–1330. https://doi.org/10.1016/j.bbamem.2015.02.025.
91. Shibagaki, N., and A. R. Grossman. 2010. Binding of Cysteine Synthase to the STAS Domain of Sulfate Transporter and Its Regulatory Consequences. *J. Biol. Chem.* 285:25094–25102. https://doi.org/10.1074/jbc.m110.126888.
92. Ko, S. B. H., W. Zeng, …, S. Muallem. 2004. Gating of CFTR by the STAS domain of SLC26 transporters. *Nat. Cell Biol.* 6:343–350. https://doi.org/10.1038/ncb1115.
93. Jiang, T., P.-C. Wen, …, E. Tajkhorshid. 2020. Computational Dissection of Membrane Transport at a Microscopic Level. *Trends Biochem. Sci.* 45:202–216. https://doi.org/10.1016/j.tibs.2019.09.001.
94. Dror, R. O., R. M. Dirks, …, D. E. Shaw. 2012. Biomolecular Simulation: A Computational Microscope for Molecular Biology. *Annu. Rev. Biophys.* 41:429–452. https://doi.org/10.1146/annurev-biophys-042910-155245.
95. Husic, B. E., and V. S. Pande. 2018. Markov state models: From an art to a science. *J. Am. Chem. Soc.* 140:2386–2396.
96. Masrati, G., R. Mondal, …, N. Ben-Tal. 2020. An angular motion of a conserved four-helix bundle facilitates alternating access transport in the TtNapA and EcNhaA transporters. *Proc. Natl. Acad. Sci. USA.* 117:31850–31860.
97. Okazaki, K.-I., D. Wöhlert, …, G. Hummer. 2019. Mechanism of the electroneutral sodium/proton antiporter PaNhaP from transition-path shooting. *Nat. Commun.* 10:1742.
98. Geertsma, E. R., Y.-N. Chang, …, R. Dutzler. 2015. Structure of a prokaryotic fumarate transporter reveals the architecture of the SLC26 family. *Nat. Struct. Mol. Biol.* 22:803–808.
99. Kuhn, B. T., J. Zöller, …, E. R. Geertsma. 2024. Interdomain-linkers control conformational transitions in the SLC23 elevator transporter UraA. *Nat. Commun.* 15:7518.
100. Jiang, T., P.-C. Wen, …, E. Tajkhorshid. 2020. Computational dissection of membrane transport at a microscopic level. *Trends Biochem. Sci.* 45:202–216.
101. Babu, M., J. F. Greenblatt, …, T. F. Moraes. 2010. Structure of a SLC26 anion transporter STAS domain in complex with acyl carrier protein: implications for E. coli YchM in fatty acid metabolism. *Structure.* 18:1450–1462.